


## ORIGINAL RESEARCH

# Noncontact estimation of the onset of ice accretion in turbofan stators

 Khalid Saleh | John Leis  | David Buttsworth

School of Engineering, University of Southern Queensland, Toowoomba, Queensland, Australia

## Correspondence

 John Leis, School of Engineering, University of Southern Queensland, Queensland, Australia.  
Email: [john.leis@usq.edu.au](mailto:john.leis@usq.edu.au)

## Present address

John Leis, School of Engineering, University of Southern Queensland, West St, Toowoomba 4350, Queensland, Australia

## Abstract

The problem of crystal ice formation inside aircraft turbine engines is well-documented, and poses a significant risk to safety. The problem is not only one of power loss in flight, but the very real possibility that a flame-out event could occur due to ice accretion on compressor stators, with potentially catastrophic outcomes. Although many instrumentation systems have been developed for wing ice detection, incipient formation of crystal ice is somewhat more difficult to detect. This is compounded by the need for a noncontact sensor which is robust to in-flight conditions. This paper proposes an approach to the detection of ice formation based on microwave transmission characteristics across the first and possibly the second stage of the compressor stator. It is shown that noncontact detection is feasible under realistic conditions. The contribution of this paper is twofold. First, the microwave transmission approach is motivated using wind tunnel measurements, and appropriate frequency bands are determined. Next, a signal processing approach involving higher-order analysis of time-frequency distribution characteristics is then put forward. Experimental results are presented to support the hypothesis that multiband detection offers a workable approach to the incipient crystal-ice detection problem.

## 1 | INTRODUCTION

It has been known for some time that crystal ice particles form a significant threat to turbofan aircraft engines [1]. The formation of ice on compressor stators, and the subsequent accretion of ice, may happen relatively quickly in conditions which are not fully understood. This continues to cause significant danger to aircraft in flight, with many events reported (for example, [2]). In this section, we place the research problem in context.

An earlier, comprehensive report on the problem [3] documented many conditions where ice accretion resulted in aircraft flight events, and suggested a detailed hypothesis of the environment which caused engine problems. A careful distinction was made between “icing” as the accretion of supercooled liquid water on aircraft surfaces, “icing conditions” meaning the environment where supercooled liquid water exists, and “ice crystal icing” to denote the accretion caused by ice particles on aircraft/engine surfaces. Such icing was found to occur near convective clouds, and aircraft had not flown through a region of high radar reflectivity. Furthermore, Rosemount ice detectors

(RID), which operate on a mechanical resonance principle, did not detect ice formation.

Pilots often reported deviating around convective clouds or strong radar returns at altitude, and post-event review of satellite imagery indicated that the probable location of the aircraft was in the vicinity of a convective storm. Engine events were found to initiate within about 30 miles of the area of maximum radar reflectivity associated with a major thunderstorm, normally associated with the area of maximum precipitation. In order to mitigate the effects of ice on engine components, air-bleed systems may be employed at the inlet guide vanes [4].

### 1.1 | Ice accretion & detection

Conventional techniques to measure ice water content in airborne environments are conveniently summarized in [5] as:

- (i) Ice particle evaporation techniques;
- (ii) Indirect power measurement approaches using hot-wire sensors;
- (iii) Determination of ice particle size distribution.

This is an open access article under the terms of the [Creative Commons Attribution-NonCommercial-NoDerivs](https://creativecommons.org/licenses/by-nc-nd/4.0/) License, which permits use and distribution in any medium, provided the original work is properly cited, the use is non-commercial and no modifications or adaptations are made.

© 2024 The Authors. *IET Science, Measurement & Technology* published by John Wiley & Sons Ltd on behalf of The Institution of Engineering and Technology.

To support sensing and measurement of volumetric ice content, theoretical models have been under development so as to inform the sensor designs. However, it is recognized that the physical basis of ice accretion is still not fully understood, especially under the physical conditions at high altitude [6]. Two main methods of formation have been identified in the literature: supercooled droplet icing (SDI) or supercooled water icing (SWI), and ice crystal icing (ICI) [7]. Ice accretion typically occurs on the exterior of the aircraft, whereas crystal ice accretion can only occur inside the aircraft engine. Additionally, crystal ice accretion is not simply a matter of cold water droplets sticking to an aircraft's surface; it requires some thermal energy for the particles to partially melt. Since solid ice particles generally do not adhere to cold surfaces, glaciated clouds present little or no danger of wing and fuselage icing [7]. Liquid droplets, however, have been described as thermodynamically metastable, with a phase change from the solid state initiated by local mechanical disturbances [7]. Conditions conducive to ice accretion have been extensively studied, and a hypothesis for accretion due to crystal ice ingestion in mixed-phase conditions was put forward in [3], wherein the presence of liquid water was suggested as a necessary condition for ice accretion. The ratio of liquid water content (LWC) to total water content (TWC) and its effects on ice accretion was studied in [8]. Mixed-phase icing studies are reported in [9]; there appears to be a critical range of LWC/TWC for optimum icing [10]. Particle size effects are further studied in [11] and [12]. More recently, a comprehensive ice crystal accretion model in the so-called glaciated icing regime was put forward in [13]. Experimental and numerical characterizations as detailed in [7], and theoretical models such as those described in [13], serve to inform the understanding of expected icing conditions in the presence of certain ambient conditions (possibly with additional physical constraints), such as temperatures and temperature gradients. This paper investigates a novel proposal for ICI detection in turbine stators, given that ICI is a significant and likely under-reported phenomenon. Although high concentrations of small ice crystals are difficult to detect by current on-board radar technology [7], the measurement modality of microwave transmission, rather than reflection, appears to offer promise if the frequency bands are carefully chosen, especially when combined with appropriate processing algorithms.

## 1.2 | Conventional ice detection approaches

For aircraft, Rosemount ice detectors are utilized as a warning system for ice accretion [14, 15]. The principle of operation is based on the resonant frequency of a physical probe, and this is augmented with periodic heating cycles. The change in the resonant frequency is used to indicate the presence of ice, using a calibrated model. However, since this requires the physical accretion of ice, it is not suitable for the problem of detecting the possible onset of crystal ice formation.

Detection and measurement of ice after formation has been reported using various novel metrological approaches, such as counting alpha particles [16] and optical fibre measurements in

the near-infrared [17]. These approaches, however, depend on actual ice accretion. The determination of ice within flows is a related but distinct problem. Different types of probe arrangement have been the subject of in-flight tests [18]. The Nevzorev probe is a hot-wire probe for measuring total water content (TWC) and liquid water content (LWC). It is based on thermodynamic models, and consists of a heater wire for each type of measurement, together with a reference wire which is shielded from direct contact with ice particles. The heating power necessary to maintain a constant temperature is determined by means of feedback [19, 20]. Although such probes are able to estimate TWC and LWC, and thus infer possible ice formation conditions, they are more suited to atmospheric research than in hostile environments such as compressor flows.

Icing probes continue to be an area of research, utilizing wind tunnel experiments [21]. As reported in [22], capture of very small ice particles using isokinetic probes may under-report actual ice content. The accretion process appears to be dependent on spongy ice accretion, for which a model was proposed in [23].

## 1.3 | The crystal ice detection problem

None of these approaches are entirely suited to the detection of incipient crystal ice formation, before actual accretion, especially in proximity to engine intakes where accretion may result in catastrophic failure modes.

Ideally, a noncontact sensor is desired. An infrared approach was reported in [24], although this requires ice accretion to have occurred. A point-source laser approach is reported in [25], utilizing 660 nm radiation and a non-collimated image. However, this approach is focussed on static structures. A video-based approach was reported in [26], although once again this required ice to have accreted.

Infrared reflectance in the band 880–920 nm with heating/cooling cycles was reported in [27]; a blue LED light transmission system was studied in [28]. Microwave snow and ice sensing systems are reported extensively in the literature, with [29] demonstrating that ultra wideband (UWB) radar in the 10 GHz region could determine changes in the dielectric conditions over a range due to changes in spectral components.

Electromagnetic approaches have recently been reported, with a passive approach in [30] and [31], and resonant cavity approaches [32]. Fundamentally, these depend on the differences in dielectric permittivity between water and ice, which is not insignificant.

## 1.4 | Microwave sensing

In order to successfully develop a reliable incipient ice crystal formation detector based on microwave absorption, two potential obstacles need to be addressed. First and most importantly, the range of frequencies which potentially provide adequate discrimination between ice and non-ice conditions need to be determined. Without these fundamental measurements, the

system is unworkable. Secondly, once band(s) have been identified, an appropriate post-processing algorithm is needed to provide reliable detection, coupled with a low false-positive alert rate. The following sections describe each of these aspects in turn.

The use of microwaves to probe physical quantities has a long history [33–35], and more recently in [36]. Measurement of microwave propagation characteristics in a furnace is reported in [37]. A microwave measurement method reported in [38] employs a novel optical modulator to detect phase changes for the purpose of modulation detection and analysis.

Specific measurements of refractive indices of ice and water are discussed in [39], with application to relative moisture content discussed in [40]. A useful compilation of physical constants appears in [41], with temperature effects [42]. The permittivity of ice is investigated in [43] and [44]. This has led to numerous practical techniques, such as for the dielectric spectroscopy of biological specimens [45] and natural gas water vapour estimation [46]. Utilization of microwave transmission active measurements has been applied to grain moisture measurement in [47] and [48]. Other allied applications in practice include the measurement of ice fraction in water [49] and steam quality [50].

## 2 | PROPOSED APPROACH

A limited number of test facilities have been constructed by various research groups for studying the crystal icing problem. Examples include [51–53] and [54].

The original experimental setup employed in the work presented here was initially described in detail in [55]. This was an early prototype of the icing wind tunnel, and significant enhancements to the ice generation, as well as instrumentation, were required for this investigation. In-flow temperature and humidity sensors were incorporated as described in [56]. Subsequent enhancements to the data acquisition and processing were undertaken, and microwave instrumentation able to capture real-time VNA (vector network analyzer) scans was designed and implemented. Improved liquid nitrogen injection for constant flow and temperature was also incorporated.

The icing wind tunnel is an open system tunnel, with two main parts: the icing jet generator and an open circuit wind tunnel, which operate in harmony. Figure 1 depicts the experimental setup from an overall perspective. The flow is from left to right, with water injected into the far left, with a liquid nitrogen (LN<sub>2</sub>) evaporation cup where ambient air is ingested to produce cooling. The portion where measurements are taken is shown in Figure 2, during an active run.

The ice generator has multiple nozzles which can produce water droplets less than 40  $\mu\text{m}$  in diameter. The quantity of water droplets is determined by the number of nozzles and the water pressure. These droplets move through a chamber of mixed cold air with liquid nitrogen vapour at  $-100\text{ }^\circ\text{C}$  for sufficient time for ice crystals to form.

Subsequently, the crystal particles travel through a perforated chamber where warm air forces the particles to stay in the mid-

dle of the chamber and become partially melted. The mix then travels through a nozzle to accelerate the ice particle to the wind tunnel speed that can be controlled up to  $50\text{ m s}^{-1}$ . The test section of the wind tunnel is accessible from all sides, and is instrumented to record temperature, pressure, and live videos of the initial stages of the icing on a real engine aerofoil or cluster of engine blades. The flow in the test section is a co-flow system, wherein the core of diameter 170 mm is the cold stream containing the second stream is the warm air drawn in to accelerate the cold stream even further, to reach to the desired speed. The aerofoil is mounted near the icing jet generator nozzle exit in the wind tunnel test section, and is illustrated in Figure 3.

### 2.1 | Microwave sensing & data capture

The microwave sweep transmits at a power level of +6 dBm over the range 5.6–5.8 GHz, and takes approximately 3.5 s. The Python code which configures the VNA is shown in Figure 4. The microwave antenna has a diameter of 70 mm, length 110 mm, and open stub of length 40 mm. Identical transmit and receive units are used across the measurement volume, with a separation of 350 mm.

The vector network analyzer (VNA) employed was a PicoVNA programmed using Python via the Pico API (Applications Programming Interface). A Python script was employed for data communications, data collection, logging and real-time graphical display of measurements. The frequency bandwidth, measurement points, and other parameters were set up as described in the Results section. The power level employed was 6 dBm, and all  $S$  parameters reported, though only the transmission parameter  $S_{12}$  is recorded and utilized here. MATLAB was utilized for post-processing and preparing analysis graphs.

### 2.2 | In-flow sensors

In order to fully instrument the system, a number of additional sensors were designed and added in order to augment the primary microwave sensor system. A carbon fibre blade was 3D printed with internal wiring cavities to accommodate on-blade sensors, which were parallel to the flow direction. A number of SHT85 combined temperature and humidity sensors were utilized, and mounted as illustrated in Figure 5. One additional SHT85 sensor was also mounted out of the flow, to sense ambient conditions. These sensors use the I<sup>2</sup>C communication protocol to return a binary representation of both temperature and humidity. The data from all of these sensors was collected by an Arduino system, with a data communications protocol reporting the sensor results in real-time to a Python script and logged to a file. The sensor address is hardwired within the sensor itself, which precluded direct connection to a processor bus. To overcome this limitation, an I<sup>2</sup>C library was developed to perform the synchronization and data transfer in software on the Arduino. A calibration algorithm is also used according to the manufacturer's data to transform the raw binary integers into usable temperature and relative humidity values.

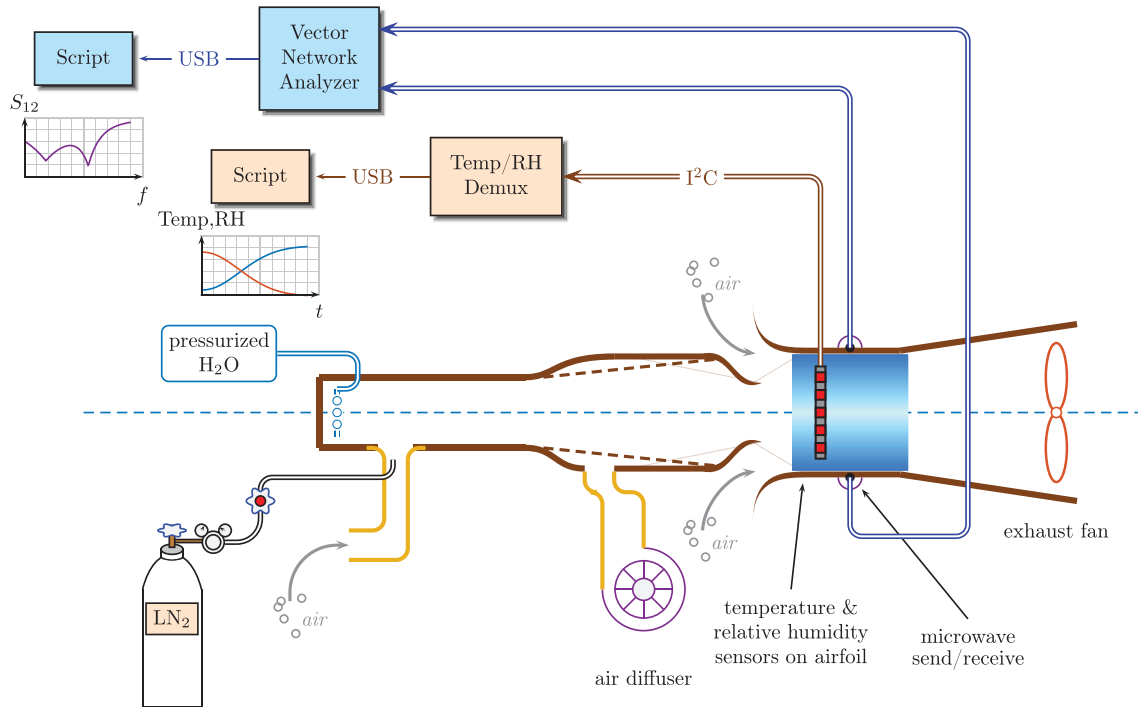


**FIGURE 1** A block diagram of the overall experimental wind tunnel facility, depicting the main components of both functional operation and instrumentation & measurement.

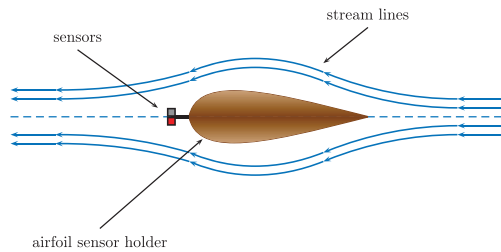


**FIGURE 2** Mounting of sensors for in-flow temperature and humidity sensors. The design goal is to have no stagnation points where ice can accumulate. Disruption of the flow is also minimized.

```
fStart = 5640
fStep = 0.2
fNumPoints = 1024*1
fBandwidth = 10
fPower = 6

picoVNACOMObj.SetFreqPlan( fStart , fStep ,
    ↪ fNumPoints, fPower, fBandwidth)
raw = picoVNACOMObj.GetData( "S12", "logmag", 0)

splitdata = raw.split(',')
cdata = np.array(splitdata)
cdata = cdata.astype(float)
frequency = cdata[:, 2]
data = cdata[:, 1 : 2]
```

**FIGURE 4** Code used to initialize the VNA parameters for microwave measurement sweeps.

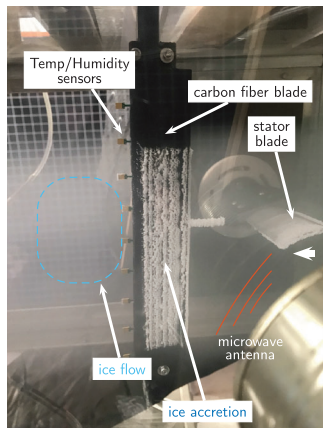


**FIGURE 3** A closeup view of the stator and instrumentation blades while ice formation is occurring.

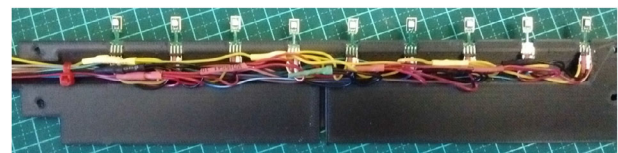


**FIGURE 5** SHT85 I<sup>2</sup>C sensors mounted on a carbon fibre blade.

### 3 | EXPERIMENTAL RESULTS

In order to place the results in context, we first describe the humidity and temperature results from a typical run. Figure 6 shows the recorded results using the on-blade SHT85 sensors.



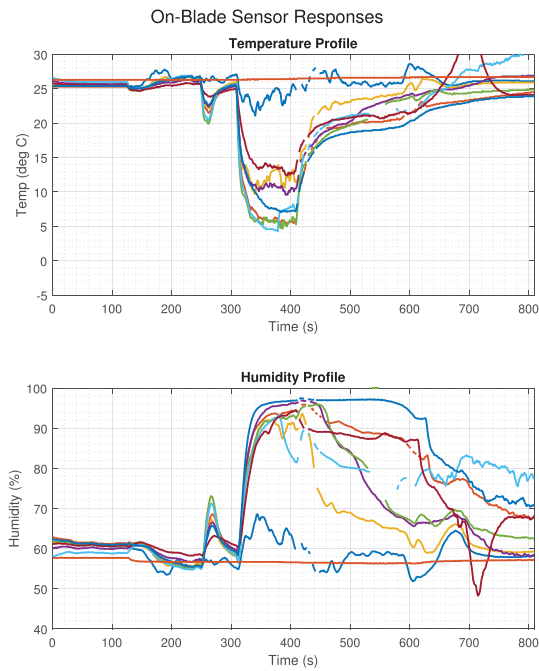


**FIGURE 6** On-blade temperature and humidity using software-multiplexed SHT85 sensors. Each trace represents one sensor output. Closer to the core of the flow, a more dramatic change in temperature and humidity is evident, as expected. The outer sensors, further away from the mixing layer, exhibit relatively less departure from the external ambient conditions.

The temperature of the wind tunnel begins at the ambient temperature. As the main wind tunnel fan is started, a small drop in temperature is evident between  $\sim 180$ – $210$  s. After the ice generator fan started at  $\sim 220$  s, the temperature of the wind tunnel core started to rise by around  $\sim 2$  °C above the room temperature due to compression in the ice generator. This continues until the liquid nitrogen injection starts, around 280 s. Steady-state injection of liquid nitrogen was reached at 340 s and from there, the wind tunnel core temperature dropped to 5 °C. The temperature variation due to the location of the sensor in the core of the wind tunnel flow is evident. The test section temperature was steady from  $\sim 350$ – $450$  s. As the liquid nitrogen is depleted, the wind tunnel temperature starts to rise again, to reach ambient temperature at  $\sim 600$  s. Figure 7 has been annotated to show the various experimental phases.

The relative humidity starts at the ambient level, and as the wind tunnel temperature slightly decreases between  $\sim 180$ – $210$  s the humidity increases. When the ice generator fan increases the wind tunnel core temperature, the relative humidity is affected as can be seen near 220 s. As the icing wind tunnel core temperature continues to decrease due to the injection of the refrigerant, the relative humidity rises significantly.

One of the humidity sensors was placed facing the core wind tunnel flow in order to run a wet test before the liquid nitrogen test, and it was observed that water droplets were lodged in the tubes leading to the sensor.

Using the abovementioned microwave sweep (VNA) approach, the same experimental run was instrumented with transmit and receive antennas across the compressor throat

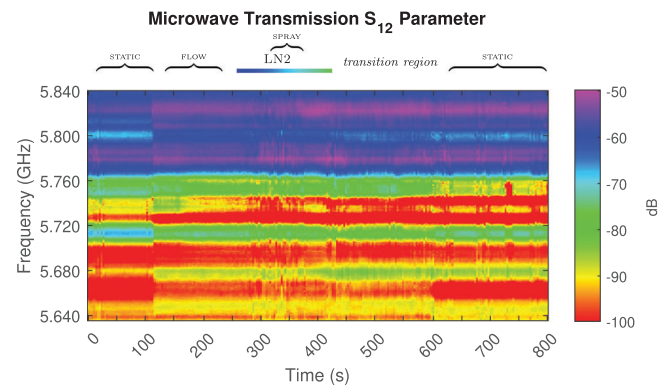


**FIGURE 7** Transmission parameter  $S_{12}$  for comparison to on-blade temperature and humidity profiles. The annotations refer broadly to the flow conditions at each stage: static refers to initial quiescent conditions; flow is when airflow is effected but no other conditions have changed; LN2 denotes the region where liquid nitrogen is injected; spray is when the water droplet spray is running; transition region denotes the transition to ice particles within the flow; finally, static is the gradual return to quiescent conditions (note that this is not immediate, due to cooling and residual water within the flow chambers).

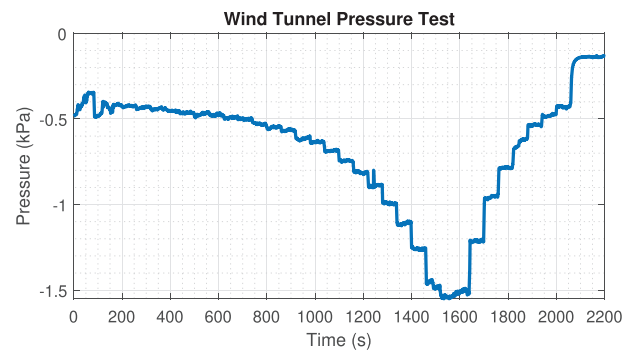


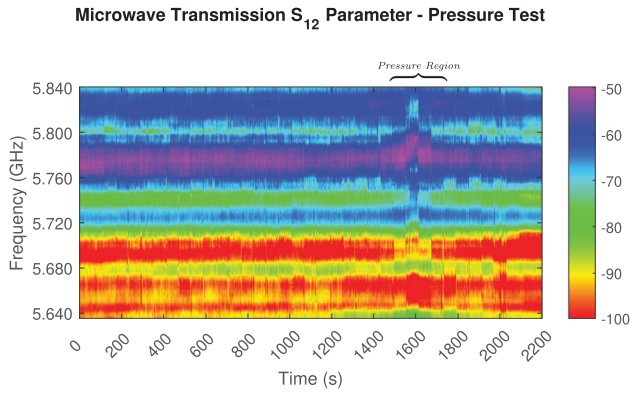
**FIGURE 8** Variation of pressure below atmospheric pressure as flow speed is increased and then decreased.

region, in the vicinity of the instrumented carbon-fibre blade. The corresponding results for microwave absorption are shown in Figure 7. This false-colour plot shows the relative log magnitude of the received signal, the  $S_{12}$  parameter. The annotations on this figure are derived from video recording and observation of the chamber, together with the thermodynamic expectations for ice formation.

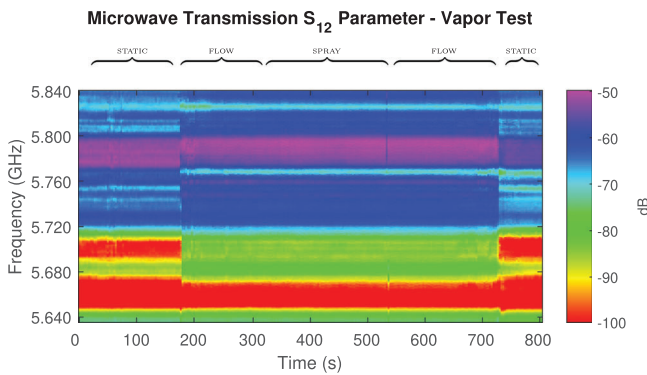
### 3.1 | Pressure-related effects

In order to account for pressure variations, an experimental run with pressure variation only was conducted. Neither water spray nor cooling are employed for these results. The tunnel coupling was initially open, then the threaded coupling was slowly closed to obtain maximum flow speed within the core. Subsequently, the coupling was reopened.

Figure 8 shows the measured pressure variation profile over time. For reference, the ambient pressure was also recorded. The test location is 690 m above sea level.



**FIGURE 9** Transmission parameter  $S_{12}$  as pressure only is varied, with temperature and humidity kept constant.



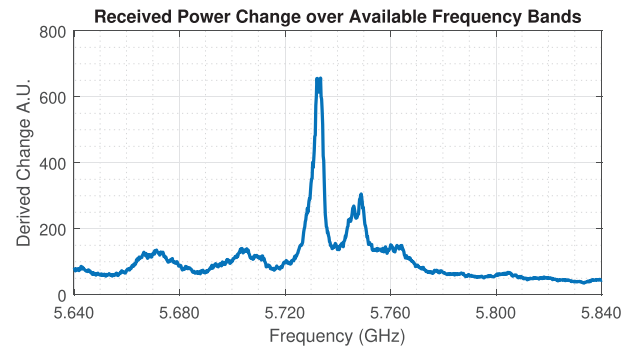
**FIGURE 10** Transmission parameter  $S_{12}$  as compressor flow is switched on, and water spray injected.

Figure 9 shows the VNA scan results for the pressure variation experiment. It is performed over the range 5.645–5.844 GHz since this is the approximate area where significant variations were found. The figure employs a false-colour rendition of the received  $S_{12}$  parameter. It is evident that certain bands exhibit measurable changes as a result of pressure variation, whereas some bands remain constant.

### 3.2 | Liquid water related effects

In order to ascertain whether water alone affects the microwave transmission, as would be expected, an experimental run recorded the  $S_{12}$  parameter when no nitrogen cooling was applied. The results are depicted in Figure 10. This figure shows the core flow times and water injection ranges.

As a result of the independent pressure and water experiments, it is clear that some variation in the microwave region is measurable. This is a complex interplay of physical parameters—for example, pressure increases also manifest temperature variations and humidity changes. It is clear that raw measurements alone are not sufficient to discriminate these conditions.



**FIGURE 11** Frequency sweep power changes over the range of interest. Narrowing the band enables a reduced sweep time, and thus faster detection.

### 3.3 | Icing onset experiments

In this section, we present the results for the microwave instrumentation which are also measured with the in-flow temperature and humidity sensors. This is done in order to more accurately determine the icing onset conditions.

From this, we can infer the most useful frequency bands for detection of ice formation. Figure 11 shows the changes across all measured frequency bands for a subsequent experimental run. It is evident that the most active region is 5.720–5.740 GHz. The narrower band is useful in practice, not only to detect the regions exhibiting the most activity, but also to reduce the measurement sweep time. A narrower sweep range enables a shorter update time for the VNA parameters.

## 4 | ICING ONSET DETECTION

In order to provide a forward estimate of the possibility of the onset of icing, it is necessary to utilize only the prior measurements. As observed in the previous discussion, although transmission parameters are affected by temperature, humidity, and pressure, it is the unique combination of these variables which provides the desired onset likelihood. More specifically, we note that the relative activity in the frequency bands as indicated precedes the formation of ice crystals.

Thus, we require an estimation regime based on signal energy characteristics over the energetic frequency bands. Define the received parameter data for each VNA measurement sweep as  $S_{12}(k, n)$ , where  $S_{12}$  represents the transmission parameter, with  $k$  the frequency band index, and  $n$  is the time block index. Since the received power (and phase) are computed using an FFT approach,  $K = 2^{10}$  FFT spectrum points were utilized with  $k = 0, 1, \dots, K - 1$ . The sweep time index is  $n = 0, 1, \dots$  with the time interval between sample blocks approximately 4 s. This is governed by the VNA sweep time, data transfer time, and data recording time—although the later are done partially in parallel.

Since we wish to use the current and past measurements to predict ice onset potential, the magnitude of the frequency-domain differences are calculated using

$$\Delta S_{12}(k, n) = |S_{12}(k, n) - S_{12}(k - 1, n)| \quad (1)$$

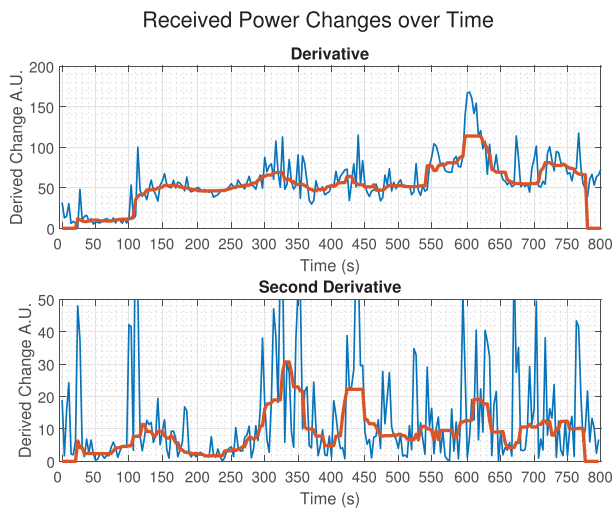


**FIGURE 12** The frequency-domain derivatives: first (top) and second (lower) differences. The blue trace shows the derivative signal, with the red trace showing the median-filtered derivative. At  $t \approx 300$  s, icing is beginning, and this is evident by the uptick in the red trace in the lower panel. At  $t \approx 400$  s, liquid nitrogen flow ceases and so the relative icing activity begins to reduce. From  $t \approx 600$  s onwards, the level of activity substantially declines, corresponding to a gradual return to ambient conditions.

The sum over all frequency bands

$$\psi(n) = \sum_{k=0}^{K-1} \Delta S_{12}(k, n) \quad (2)$$

is shown in Figure 12, together with the corresponding second-difference estimate

$$\Delta\psi(n) = |\psi(n) - \psi(n-1)| \quad (3)$$

Due to the inherent highpass nature of the simple-difference estimates, the underlying trend is difficult to observe. To derive a smoother estimate, either an improved highpass filter is possible, or correspondingly, lowpass filtering of the derivatives. However, the median filter is known to produce good results for impulsive noise in other contexts such as image processing.

The ability of image filters to preserve edges in images, in the presence of impulsive noise, is an important motivator in the present context. Just as the sample mean is the maximum likelihood (ML) estimator of independent, identically distributed (iid) samples with an underlying Gaussian distribution, the sample median is the ML estimator for iid Laplacian samples. In the former case, the mean minimizes the mean-square error of the estimator, whereas in the latter case the median minimizes the absolute error [57].

Median filtering is applied to both the first and second order difference signals, with a window size of  $W = 17$ , as shown in Figure 12. The ice formation regions are indicated by a combination of both median-filtered components. The first derivative alone is not able to discriminate the ice formation stage, however the median-filtered second derivative is able to provide a useful indicator of the ice formation conditions occurring.

## 5 | DISCUSSION

Figure 12 indicates that the first-order difference is a reasonable proxy for many conditions which may, independently, indicate incipient ice formation. However, the second-order differences are a more reliable indicator of incipient ice formation. This is evident when comparing Figure 12 with the annotated time-bar shown in Figure 7.

Both first second derivatives show evidence of the start of the flow at  $\sim 100$  s. Subsequently, when the liquid nitrogen is injected, both the VNA sweep and the filtered second derivative indicate the change in conditions. Crystal ice particles start to travel in the test section at  $\sim 300$  s, and the first derivative shows some sensitivities to the flow in the test section. However, the second derivative of the signal shows significant sensitivities to the particles. Beyond  $\sim 450$  s, only the residual crystal particles in the icing jet generator remain, slowly decaying over time.

## 6 | CONCLUSION

This paper has introduced the notion of a non-contact incipient ice detection sensor based on microwave absorption measurements. The rates of change of power transmission in the frequency domain were observed to be somewhat related to the formation of ice. Furthermore, the relative change of the second derivative was found to be a useful indicator of the desired target parameter. Due to the small signal levels employed, and the considerable reflections in the frequency bands utilized, filtering of the estimates was found to be essential in order to produce meaningful results. The resulting system shows good agreement both with in-flow measurements and expectations derived from thermodynamic considerations.

## AUTHOR CONTRIBUTIONS

**Khalid Saleh:** Data curation; investigation; methodology; validation; writing—original draft; writing—review and editing. **John Leis:** Data curation; investigation; methodology; resources; software; writing—original draft; writing—review and editing. **David Buttsworth:** Conceptualization; funding acquisition; investigation; methodology; resources; validation; writing—review and editing.

## ACKNOWLEDGMENTS

Open access publishing facilitated by University of Southern Queensland, as part of the Wiley - University of Southern Queensland agreement via the Council of Australian University Librarians.

## CONFLICTS OF INTEREST STATEMENT

The authors declare no conflicts of interest.

## DATA AVAILABILITY STATEMENT

Data available on request from the authors.

## ORCID

John Leis  <https://orcid.org/0000-0001-5930-8139>



## REFERENCES

1. Lawson, R.P., Angus, L.J., Heymsfield, A.J.: Cloud particle measurements in thunderstorm anvils and possible weather threat to aviation. *J. Aircr.* 35(1), 113–121 (1998). <https://doi.org/10.2514/2.2268>
2. SKYbrary Aviation Safety: MD83, en route, near Gossi Mali, 2014. SKYbrary Aviation Safety. <https://skybrary.aero/accidents-and-incidents/md83-en-route-near-gossi-mali-2014> (2014). Accessed 23 March 2024
3. Mason, J., Strapp, W., Chow, P.: The ice particle threat to engines in flight. In: 44th AIAA Aerospace Sciences Meeting and Exhibit, pp. 1–21. AIAA Press, Reston, VA (2006)
4. Li, L., Liu, Y., Tian, L., Hu, H., Hu, H., Liu, X., Hogate, I., Kohli, A.: An experimental study on a hot-air-based anti-/de-icing system for aero-engine inlet guide vanes. *Appl. Therm. Eng.* 167, 114778 (2020). <https://www.sciencedirect.com/science/article/pii/S1359431119353694>
5. Abel, S.J., Cotton, R.J., Barrett, P.A., Vance, A.K.: A comparison of ice water content measurement techniques on the FAAM BAe-146 aircraft. *Atmos. Meas. Tech.* 7(9), 3007–3022 (2014). <https://amt.copernicus.org/articles/7/3007/2014/>
6. Gloerfeld, M., Schreimb, M., Criscione, A., Jakirlic, S., Tropea, C.: Impact of supercooled drops onto cold surfaces. In: Schulte, K., Tropea, C., Weigand, B. (eds.) *Droplet Dynamics Under Extreme Ambient Conditions*, pp. 311–329. Springer Nature, Cham (2022)
7. Baumert, A., Bansmer, S., Trontin, P., Villedieu, P.: Experimental and numerical investigations on aircraft icing at mixed phase conditions. *Int. J. Heat Mass Transfer* 123, 957–978 (2018)
8. Struk, P., Currie, T., Wright, W.B., Knezevici, D.C., Fuleki, D., Broeren, A., Vargas, M., Tsao, J.C.: Fundamental ice crystal accretion physics studies. In: SAE 2011 International Conference on Aircraft and Engine Icing and Ground Deicing, SAE International, Warrendale, PA (2011)
9. Currie, T., Struk, P., Tsao, J.C., Fuleki, D., Knezevici, D.: Fundamental study of mixed-phase icing with application to ice crystal accretion in aircraft jet engines. In: 4th AIAA Atmospheric and Space Environments Conference, pp. 523–539. AIAA Press, Reston, VA (2012)
10. Currie, T.C., Fuleki, D., Knezevici, D.C., MacLeod, J.D.: Altitude scaling of ice crystal accretion. In: 5th AIAA Atmospheric and Space Environments Conference, p. 1. AIAA Press, Reston, VA (2013)
11. Knezevici, D., Fuleki, D., Currie, T., MacLeod, J.: Particle size effects on ice crystal accretion. In: 4th AIAA Atmospheric and Space Environments Conference, p. 1. AIAA Press, Reston, VA (2012). <https://arc.aiaa.org/doi/abs/10.2514/6.2012-3039>
12. Knezevici, D.C., Fuleki, D., Currie, T.C., Galeote, B., Chalmers, J., MacLeod, J.D.: Particle size effects on ice crystal accretion - part II. In: 5th AIAA Atmospheric and Space Environments Conference, p. 1. AIAA Press, Reston, VA (2013)
13. Trontin, P., Villedieu, P.: A comprehensive accretion model for glaciated icing conditions. *Int. J. Multiphase Flow* 108, 105–123 (2018)
14. Claffey, K.J., Jones, K.F., Ryerson, C.C.: Use and calibration of rosemount ice detectors for meteorological research. *Atmos. Res.* 36(3), 277–286 (1995)
15. National Center for Atmospheric Research: An evaluation of the rosemount ice detector for aircraft hazard warning and for undercooled cloud water content measurements. National Center for Atmospheric Research/University Corporation for Atmospheric Research. <https://opensky.ucar.edu/islandora/object/technotes:270> (1981). Accessed 23 March 2024
16. Bakhom, E.G., Cheng, M.H.M., Van Landingham, K.M.: Alpha-particle-based icing detector for aircraft. *IEEE Trans. Instrum. Meas.* 63(1), 185–191 (2014)
17. Li, W., Zhang, J., Ye, L., Zhang, H.: A fiber-optic solution to aircraft icing detection and measurement problem. In: 2009 International Conference on Information Technology and Computer Science, vol. 1, pp. 357–360. IEEE, Piscataway, NJ (2009)
18. Gerber, H., Twohy, C.H., Gandrud, B., Heymsfield, A.J., McFarquhar, G.M., DeMott, P.J., Rogers, D.C.: Measurements of wave-cloud microphysical properties with two new aircraft probes. *Geophys. Res. Lett.* 25(8), 1117–1120 (1998). <https://agupubs.onlinelibrary.wiley.com/doi/abs/10.1029/97GL03310>
19. Korolev, A.V., Strapp, J.W., Isaac, G.A., Nevzorov, A.N.: The nevzorov airborne hot-wire LWC-TWC probe: principle of operation and performance characteristics. *J. Atmos. Oceanic Technol.* 15(6), 1495–1510 (1998). [https://doi.org/10.1175/1520-0426\(1998\)015<1495:TNAHWL>2.0.CO;2](https://doi.org/10.1175/1520-0426(1998)015<1495:TNAHWL>2.0.CO;2)
20. Korolev, A., Strapp, J., Isaac, G., Emery, E.: Improved airborne hot-wire measurements of ice water content in clouds. *J. Atmos. Oceanic Technol.* 30, 2121–2131 (2013)
21. Davison, C.R., MacLeod, J.D.: Characterization of an engine icing tunnel and comparison to liquid water content from an evaporation mode. In: 2018 Atmospheric and Space Environments Conference, AVIATION Forum, American Institute of Aeronautics and Astronautics, p. 1. AIAA Press, Reston, VA (2018).
22. Lilie, L., Davison, C., Ratvasky, T.: Naturally aspirating isokinetic total water content probe: wind tunnel test results and design modifications. In: SAE 2011 International Conference on Aircraft and Engine Icing and Ground Deicing, p. 1. SAE International, Warrendale, PA (2011)
23. Lian, W., Zhao, L., Xuan, Y., Shen, J.: A modified spongy icing model considering the effect of droplets retention on the ice accretion process. *Appl. Therm. Eng.* 134, 54–61 (2018)
24. Du, C., Wang, Q., Liu, X., Zhao, Y., Deng, X., Cui, L.: Research and application of ice thickness and snow depth automatic monitoring system. *IEEE Trans. Instrum. Meas.* 66(2), 325–331 (2017)
25. Molkoselkä, E.O., Kaikkonen, V.A., Mäkynen, A.J.: Measuring atmospheric icing rate in mixed-phase clouds using filtered particle data. *IEEE Trans. Instrum. Meas.* 70, 1–8 (2021)
26. Wang, B., Ma, F., Ge, L., Ma, H., Wang, H., Mohamed, M.A.: Icing-EdgeNet: a pruning lightweight edge intelligent method of discriminative driving channel for ice thickness of transmission lines. *IEEE Trans. Instrum. Meas.* 70, 1–12 (2021)
27. Rydblom, S., Thörnberg, B.: Measurement of atmospheric icing and droplets. *IEEE Trans. Instrum. Meas.* 69(8), 5799–5809 (2020)
28. Rydblom, S., Thörnberg, B., Olsson, E.: Field study of LWC and MVD using the droplet imaging instrument. *IEEE Trans. Instrum. Meas.* 68(2), 614–622 (2019)
29. Rodriguez-Morales, F., Leuschen, C., Carabajal, C.L., Paden, J., Wolf, J.A., Garrison, S., McDaniel, J.W.: An improved UWB microwave radar for very long-range measurements of snow cover. *IEEE Trans. Instrum. Meas.* 69(10), 7761–7772 (2020)
30. Faulkner, C.D., Herrera, B., Jean, B.R., McClain, S.T.: Improved electromagnetic sensor for detection of ice accretion inside turbofan engine axial compressor stages. In: 2018 Atmospheric and Space Environments Conference, p. 1. AIAA Press, Reston, VA (2018)
31. Trapp, T.J., Shannon, T.A., Herrera, B.J., Jean, B.R., McClain, S.T.: Electromagnetic sensor for detection of ice accretion inside turbofan jet engines. In: 9th AIAA Atmospheric and Space Environments Conference, pp. 841–850. AIAA Press, Reston, VA (2017)
32. Kozak, R., Wiltshire, B.D., Khandoker, M.A.R., Golovin, K., Zarifi, M.H.: Modified microwave sensor with a patterned ground heater for detection and prevention of ice accumulation. *ACS Appl. Mater. Interfaces* 12(49), 55483–55492 (2020). <https://doi.org/10.1021/acsami.0c17173>
33. Nicolson, A.M., Ross, G.F.: Measurement of the intrinsic properties of materials by time-domain techniques. *IEEE Trans. Instrum. Meas.* 19(4), 377–382 (1970)
34. Weir, W.B.: Automatic measurement of complex dielectric constant and permeability at microwave frequencies. *Proc. IEEE* 62(1), 33–36 (1974)
35. Afsar, M.N., Birch, J.R., Clarke, R.N., Chantry, G.W.: The measurement of the properties of materials. *Proc. IEEE* 74(1), 183–199 (1986)
36. Artemov, V.G., Volkov, A.A.: Water and ice dielectric spectra scaling at 0°C. *Ferroelectrics* 466(1), 158–165 (2014)
37. Korhonen, I., Ahola, J.: Microwave spectra inside the combustion chamber of a kraft recovery boiler – effects on communications. *IET Sci. Meas. Technol.* 11(6), 740–745 (2017). <https://ietresearch.onlinelibrary.wiley.com/doi/abs/10.1049/iet-smt.2016.0384>
38. Zhang, X., Cheng, P., Ci, Y., Tian, S.: Microwave frequency measurement method using microwave phase detection. *IET Sci. Meas. Technol.* 10(3), 234–238 (2016). <https://ietresearch.onlinelibrary.wiley.com/doi/abs/10.1049/iet-smt.2015.0086>



39. Ray, P.S.: Broadband complex refractive indices of ice and water. *Appl Opt.* 11(8), 1836–1844 (1972)
40. Kraszewski, A.W., Nelson, S.O.: Microwave resonator for sensing moisture content and mass of single wheat kernels. *Can. Agric. Eng.* 36, 611–617 (1994)
41. Warren, S.G., Brandt, R.E.: Optical constants of ice from the ultraviolet to the microwave: A revised compilation. *J. Geophys. Res. Atmos.* 113(D14), 1–10 (2008). <https://agupubs.onlinelibrary.wiley.com/doi/abs/10.1029/2007JD009744>
42. Matsuoka, T., Fujita, S., Mae, S.: Effect of temperature on dielectric properties of ice in the range 5–39 GHz. *J. Appl. Phys.* 80(10), 5884–5890 (1996). <https://doi.org/10.1063/1.363582>
43. Bohleber, P., Wagner, N., Eisen, O.: Permittivity of ice at radio frequencies: part I. coaxial transmission line cell. *Cold Reg. Sci. Technol.* 82, 56–67 (2012). <http://www.sciencedirect.com/science/article/pii/S0165232X12001127>
44. Bohleber, P., Wagner, N., Eisen, O.: Permittivity of ice at radio frequencies: part II. artificial and natural polycrystalline ice. *Cold Reg. Sci. Technol.* 83–84, 13–19 (2012). <http://www.sciencedirect.com/science/article/pii/S0165232X12001103>
45. Popovic, D., McCartney, L., Beasley, C., Lazebnik, M., Okoniewski, M., Hagness, S.C., Booske, J.: Precision open-ended coaxial probes for in vivo and ex vivo dielectric spectroscopy of biological tissues at microwave frequencies. *IEEE Trans. Microwave Theory Tech.* 53(5), 1713–1722 (2005)
46. Leontakianakos, A.N.: Determination of water vapor by microwave spectroscopy with application to quality control of natural gas. *IEEE Trans. Instrum. Meas.* 41(3), 370–374 (1992)
47. Nelson, S., Kraszewski, A.W.: Grain moisture content determination by microwave measurements. *Trans. ASAE* 33, 1303–1305 (1990)
48. Digman, M.F., Conley, S.P., Lauer, J.G.: Evaluation of a microwave resonator for predicting grain moisture independent of bulk density. *Appl. Eng. Agric.* 28, 611–617 (2012). <http://elibrary.asabe.org/abstract.asp?aid=42073&t=3>
49. Hales, A., Quarini, G., Hilton, G., Ash, D., Lucas, E., McBryde, D., Yun, X.: Ice fraction measurement of ice slurries through electromagnetic attenuation. *Int. J. Refrig.* 47, 98–104 (2014)
50. Jean, B.R.: A microwave sensor for steam quality. *IEEE Trans. Instrum. Meas.* 57(4), 751–754 (2008)
51. Steen, L.E., Ide, R.F., Zante, J.F.V., Acosta, W.J.: NASA Glenn Icing Research Tunnel: 2014 and 2015 Cloud Calibration Procedures and Results. NASA, Washington, D.C. (2015).
52. Ide, R.F., Sheldon, D.W.: 2006 Icing Cloud Calibration of the NASA Glenn Icing Research Tunnel. NASA, Washington, D.C. (2008)
53. Struk, P., Bartkus, T., Tsao, J.C., Currie, T., Fuleki, D.: Ice Accretion Measurements on an Airfoil and Wedge in Mixed-Phase Conditions. NASA, Washington, D.C. (2015)
54. Mason, J.G., Chow, P., Fuleki, D.M.: Understanding ice crystal accretion and shedding phenomenon in jet engines using a rig test. *J. Eng. Gas Turbines Power* 133(4), 041201 (2011)
55. Saeed, R., Saleh, K., Buttsworth, D.: Ice crystal icing wind tunnel at USQ: initial characterisation. In: International Society for Air-Breathing Engines. pp. 1–8. ISABE, Indianapolis, IN (2019).
56. Saleh, K., Leis, J., Buttsworth, D.: Wind tunnel for investigation of ice accretion. In: 19th Australian International Aerospace Congress, 2021 (AIAC19), pp. 311.1–311.7. Australian International Aerospace Congress, Melbourne, Victoria (2021)
57. Arce, G.R.: A general weighted median filter structure admitting negative weights. *IEEE Trans. Signal Process.* 46(12), 3195–3205 (1998)

**How to cite this article:** Saleh, K., Leis, J., Buttsworth, D.: Noncontact estimation of the onset of ice accretion in turbofan stators. *IET Sci. Meas. Technol.* 1–9 (2024). <https://doi.org/10.1049/smt2.12191>